Discovery and characterization of two Neptune-mass planets orbiting HD 212729 with TESS

David Armstrong, Ares Osborn, Vardan Adibekyan, Elisa Delgado-Mena, Saeed Hojjatpanah, Steve Howell, Sergio Hoyer, Henrik Knierim, Sérgio Sousa, Keivan Stassun, et al.

Monthly Notices of the ROYAL ASTRONOMICAL SOCIETY

MNRAS **524,** 5804–5816 (2023) https://doi.org/10.1093/mnras/stad2183
Advance Access publication 2023 July 20

Discovery and characterization of two Neptune-mass planets orbiting HD 212729 with *TESS*

David J. Armstrong [1,2★] Ares Osborn [1,2] Vardan Adibekyan,[3] Elisa Delgado-Mena,[3] Saeed Hojjatpanah,[4] Steve B. Howell,[5] Sergio Hoyer [4] Henrik Knierim,[6] Sérgio G. Sousa [3] Keivan G. Stassun [7] Dimitri Veras [1,2,8] David R. Anderson,[1,2] Daniel Bayliss,[1,2] François Bouchy,[9] Christopher J. Burke,[10] Jessie L. Christiansen,[11] Xavier Dumusque,[9] Marcelo Aron Fetzner Keniger,[1,2] Andreas Hadjigeorghiou,[1,2] Faith Hawthorn,[1,2] Ravit Helled,[6] Jon M. Jenkins,[5] David W. Latham,[12] Jorge Lillo-Box,[13] Louise D. Nielsen,[14] Hugh P. Osborn,[15] José Rodrigues,[3] David Rodriguez,[16] Nuno C. Santos,[3,17] Sara Seager,[10,18,19] Paul A. Strøm,[1,2] Guillermo Torres,[12] Joseph D. Twicken,[5,20] Stephane Udry,[9] Peter J. Wheatley[1,2] and Joshua N. Winn[21]

Affiliations are listed at the end of the paper

Accepted 2023 July 14. Received 2023 July 12; in original form 2023 June 27

ABSTRACT

We report the discovery of two exoplanets orbiting around HD 212729 (TOI 1052, TIC 317060587), a $T_{\rm eff} = 6146$ K star with V = 9.51 observed by *TESS* in Sectors 1 and 13. One exoplanet, TOI-1052b, is Neptune-mass and transits the star, and an additional planet TOI-1052c is observed in radial velocities but not seen to transit. We confirm the planetary nature of TOI-1052b using precise radial velocity observations from HARPS and determined its parameters in a joint RV and photometry analysis. TOI-1052b has a radius of $2.87^{+0.29}_{-0.24}$ $R_\oplus$, a mass of 16.9 ± 1.7 $M_\oplus$, and an orbital period of 9.14 d. TOI-1052c does not show any transits in the *TESS* data, and has a minimum mass of $34.3^{+4.1}_{-3.7}$ $M_\oplus$ and an orbital period of 35.8 d, placing it just interior to the 4:1 mean-motion resonance. Both planets are best fit by relatively high but only marginally significant eccentricities of $0.18^{+0.09}_{-0.07}$ for planet b and $0.24^{+0.09}_{-0.08}$ for planet c. We perform a dynamical analysis and internal structure model of the planets as well as deriving stellar parameters and chemical abundances. The mean density of TOI-1052b is $3.9^{+1.7}_{-1.3}$ g cm^{-3} consistent with an internal structure similar to Neptune. A nearby star is observed in *Gaia* DR3 with the same distance and proper motion as TOI-1052, at a sky projected separation of ~1500 au, making this a potential wide binary star system.

Key words: planets and satellites: detection – planets and satellites: individual: (TOI-1052, TIC 317060587).

1 INTRODUCTION

The Transiting Exoplanet Survey Satellite (*TESS*), launched in April 2018, has discovered more than 6000 exoplanet candidates and more than 300 confirmed exoplanets to date (Ricker et al. 2015), (see NASA Exoplanet Archive, Akeson et al. 2013). *TESS* has observed nearly the entire sky, in a series of 27-d sectors, with many stars observed for two or more sectors.

This large number of candidates is made up of both real exoplanets and false positives. High resolution and stable spectroscopy for radial velocity measurements is essential not only to confirm the candidate exoplanets but also to measure the mass of the planet precisely. Knowing both mass and radius of a planet provides us an estimation of the bulk density, internal structure, and planetary composition. High resolution spectroscopy allows us to fully derive stellar parameters and chemical abundances allowing studies of planetary origin, formation, and evolution (Alibert et al. 2010, 2015).

The discovery of thousands of exoplanets over recent years has revealed a diverse population of exoplanets ranging from Earth-mass to Jupiter-mass, which also can be categorized in various sub-types including hot-Jupiters and super-Earths. A less well known group is the Neptunian exoplanets, raising questions about their overall occurrence, and an apparent lack of short period Neptune-mass exoplanets – the so-called Neptunian desert (Szabó & Kiss 2011; Mazeh, Holczer & Faigler 2016) which could be due to tidal disruption and photoevaporation (Beaugé & Nesvorný 2013; Mazeh et al. 2016), combined with potential migration of evaporating planets (Boué et al. 2012). Different programs including our NCORES and NOMADS HARPS large programs aim at a more detailed investigation of Neptunian planets, and have successfully discovered several such exoplanets (e.g. Nielsen et al. 2020; Hoyer et al. 2021; Otegi et al. 2021). The number of discoveries in this parameter space remains low and more exoplanets are needed to better understand the population.

In this paper we report the discovery and confirmation of TOI-1052 b, a Neptune-like planet orbiting HD 212729, a G0 high-proper motion southern star with a visual magnitude of 9.51 (*TESS* mag of

★ E-mail: d.j.armstrong@warwick.ac.uk

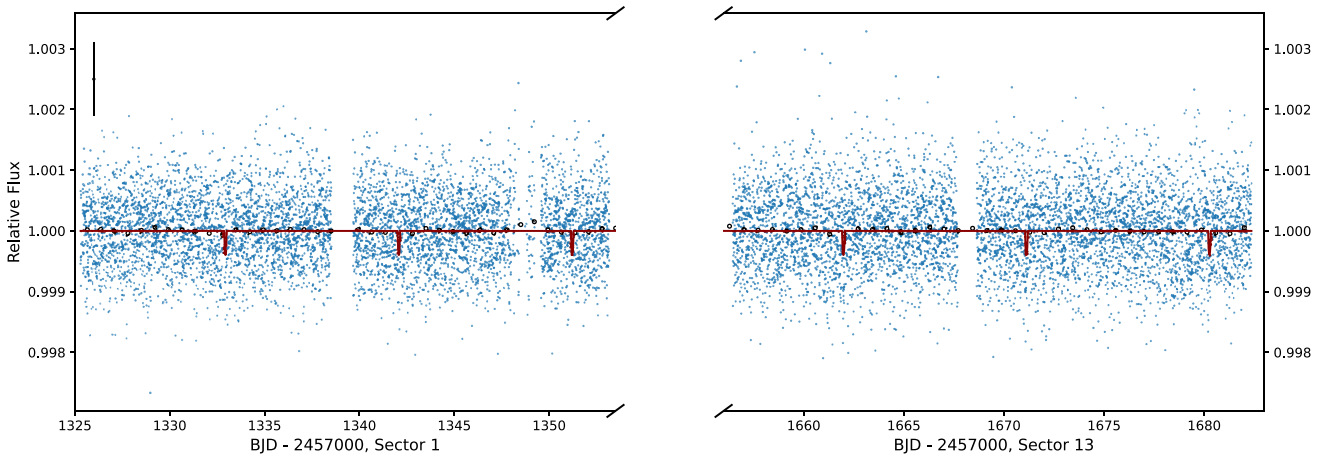

Figure 1. Full *TESS* PDCSAP light curve of TOI-1052 at 2-min cadence with the best fit model overplotted in red. A typical error bar is shown in the top left. Binned data points of width 0.7d are shown.

9.02), and a non-transiting additional planet. We use high-precision radial velocity (RV) measurements from the High Accuracy Radial velocity Planet Searcher spectrograph (HARPS, Pepe et al. 2002) mounted at the ESO La Silla 3.6-m telescope, in the framework of the NCORES program (e.g. Armstrong et al. 2020; Nielsen et al. 2020). Simultaneous analysis of the HARPS RV measurements using high resolution spectroscopy and *TESS* photometry enable us to confirm the nature of the planets as well as determine the stellar parameters of the host star.

The paper is organized as follows: the observations and data of the system are described in Section 2. The stellar parameters and signal analysis are described in Section 3. In Section 4, we describe the joint model and the discussion is presented in Section 5.

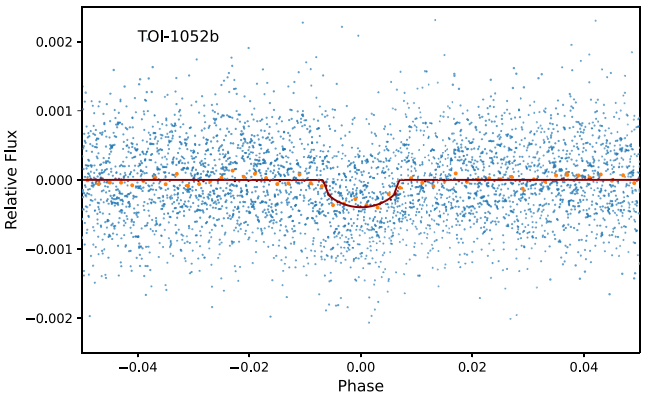

Figure 2. Fig. 1 data phase-folded on the best-fitting period for TOI-1052 b with the best fit model overplotted. Binned data points of width 0.002 in phase are shown.

2 OBSERVATIONS

2.1 *TESS* photometry

TESS observed TOI 1052 (TIC 317060587) in Sectors 1 and 13, obtaining data from 2018 July 25 to August 22 and from 2019 June 19 to 17 July. The data were reduced in the *TESS* Science Processing Operations Centre (SPOC, Jenkins et al. 2016) pipeline. This pipeline is adapted from Kepler mission pipeline at NASA Ames Research Centre (Jenkins et al. 2010a). Transit events with 9.1 d orbital period were detected in the SPOC search of the 2-min cadence light curve for Sector 1 on 2018 August 28 and for Sector 13 on 2019 July 27 with an adaptive, noise-compensating matched filter (Jenkins 2002; Jenkins et al. 2010b, 2020). A limb-darkened transit model was fitted (Li et al. 2019) and a suite of diagnostic tests were conducted to assess the planetary nature of the signal (Twicken et al. 2018). The *TESS* Science Office (TSO) reviewed the SPOC data validation reports and issued an alert for TOI 1052.01 following the Sector 13 transit search on 2019 August 16 (Guerrero et al. 2021). In a search of the combined data from both sectors, the SPOC reported a signal-to-noise ratio (SNR) of 10.62 and transit depth value of 358.4 + –33.7 parts-per-million (ppm) for the 9.14-d period transit event. The transit signal passed all diagnostic tests, and the source was localized within 2.12 + / –4.55" of the target star.

We used the publicly available Pre-search Data Conditioning Simple Aperture Photometry (PDC-SAP, Twicken et al. 2010; Smith et al. 2012; Stumpe et al. 2012, 2014) light curves provided by the SPOC for the transit modelling. Fig. 1 shows the 2 min cadence *TESS* light curve, and Fig. 2 shows the phase-folded curve for TOI 1052b. We also identified the 9.14-d transit event independently using the Transit Least Squares (TLSs) algorithm Hippke & Heller (2019) with a Signal detection efficiency (SDE) of 19.67. No further significant periodic signal was detected in the light curve.

Following Aller et al. (2020) we searched for sources of flux contamination by over-plotting the *Gaia* DR3 catalogue to the *TESS* Target Pixel Files (TPFs), shown in Fig. 3. According to *Gaia* DR3 (Gaia Collaboration et al. 2022), one star exists inside the *TESS* aperture in addition to TOI-1052 (*Gaia* DR3 6357524189130821376), with a magnitude contrast in the *Gaia* pass-band of 5.38, leading to negligible dilution of the transit. The nearby star is separated from TOI-1052 by 11.51", is at a distance of 128.9 pc consistent with the distance to TOI-1052, and has similar proper motion to TOI-1052 as shown by the proper motion vectors in Fig. 3. As such, the stars potentially form a bound system with a projected sky separation of ~1500 au. The secondary star has a temperature of 3600 K derived from the *Gaia* passbands (Fouesneau et al. 2022).

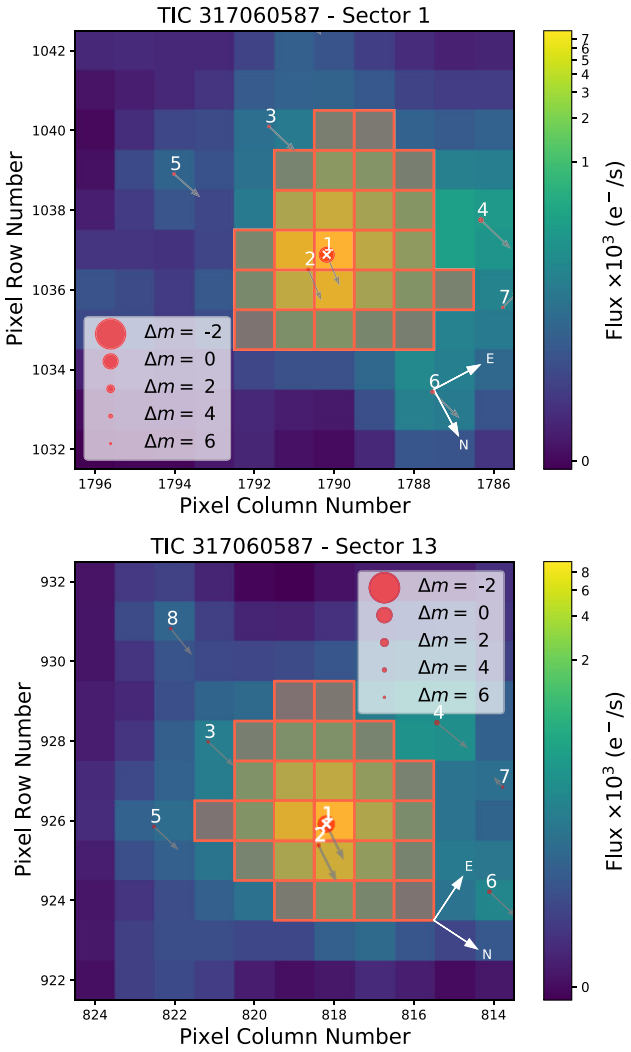

Figure 3. *TESS* pixel data with *Gaia* DR3 data sources overplotted in sector 1 (top) and 13 (bottom). TOI-1052 is marked with a white cross and the magnitude contrast is shown as red circles. Arrows show the proper motion of each star. Aperture pixels are highlighted in red. Star 2 is a potential bound companion to TOI-1052 with consistent distance and proper motion.

2.2 High-resolution imaging

TOI-1052 was observed on 2021 July 07 UT using the Zorro speckle instrument on the Gemini South 8-m telescope (Scott et al. 2021; Howell & Furlan 2022). Zorro provides simultaneous speckle imaging in two bands (562 nm and 832 nm) with output data products including a reconstructed image with robust contrast limits on companion detections. Five sets of 1000 × 0.06 s images were obtained at 832 nm only and processed in the standard reduction pipeline (see Howell et al. 2011). TOI-1052 was found to have no close companions within the angular and 5σ contrast limits (5–7 magnitudes below the target star) achieved by the observations (see Fig. 4). The angular limits from the 8-m Gemini telescope range from the diffraction limit (20 mas) out to 1.2". At the distance of TOI-1052 (d = 129.8 pc) these angular limits correspond to spatial limits of 2.6 – 155.8 au.

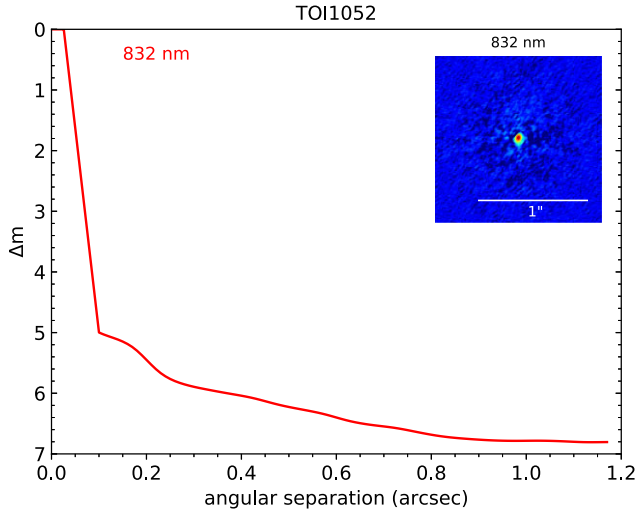

Figure 4. 5σ contrast curve for high-resolution imaging observations with Zorro/Gemini. The 832 nm reconstructed image is shown in the upper right.

2.3 HARPS follow-up

We collected 53 HARPS high-resolution spectra of TOI-1052 in three observation programmes, between 2021 May 24 and 2021 September 22. The spectrograph is mounted at the ESO 3.6-m telescope at La Silla Observatory, Chile (Mayor et al. 2003) and optimized to measure high-precision RVs. The observations were carried out as part of the NCORES large program (46 obs, ID 1102.C-0249, PI: Armstrong), with supplementary observations from the NGTS-HARPS Program (5 obs, ID 0105.C-0773(A), PI: Wheatley) and the Small planets inside and out program (2 obs, ID: 1106.C-0597(A), PI: Gandolfi).

We used the HARPS Data Reduction Software (DRS) to reduce the data, using a G0 template in order to measure RVs using a cross-correlation function (CCF) (Baranne et al. 1996; Pepe et al. 2002). The spectrum signal-to-noise ratio (SNR) is approx. 40 per pixel leading to a mean photon-noise uncertainty of 2.06 m s^{-1}. The DRS was used to measure the full width half maximum (FWHM), the line bisector, and the contrast of the CCF, as well as several activity indicators. The mean $log(R'_{HK})$ of the star is -5.32 ± 0.02 implying a relatively low-magnetic activity level.

The full RV timeseries is shown in Fig. 5.

3 HOST STAR FUNDAMENTAL PARAMETERS

3.1 Spectroscopic analysis

The stellar spectroscopic parameters ($T_{\rm eff}$, log g, microturbulence, [Fe/H]) were estimated using the ARES + MOOG methodology. The methodology is described in detail in Santos et al. (2013); Sousa (2014); Sousa et al. (2021). To consistently measure the equivalent widths (EWs) we used the latest version of ARES[1] (Sousa et al. 2007, 2015). The list of iron lines is the same as the one presented in Sousa et al. (2008). For this we used a co-added HARPS spectrum of TOI-1052. In this analysis we use a minimization process to

[1]The latest version, ARES v2, can be downloaded at https://github.com/sousasag/ARES

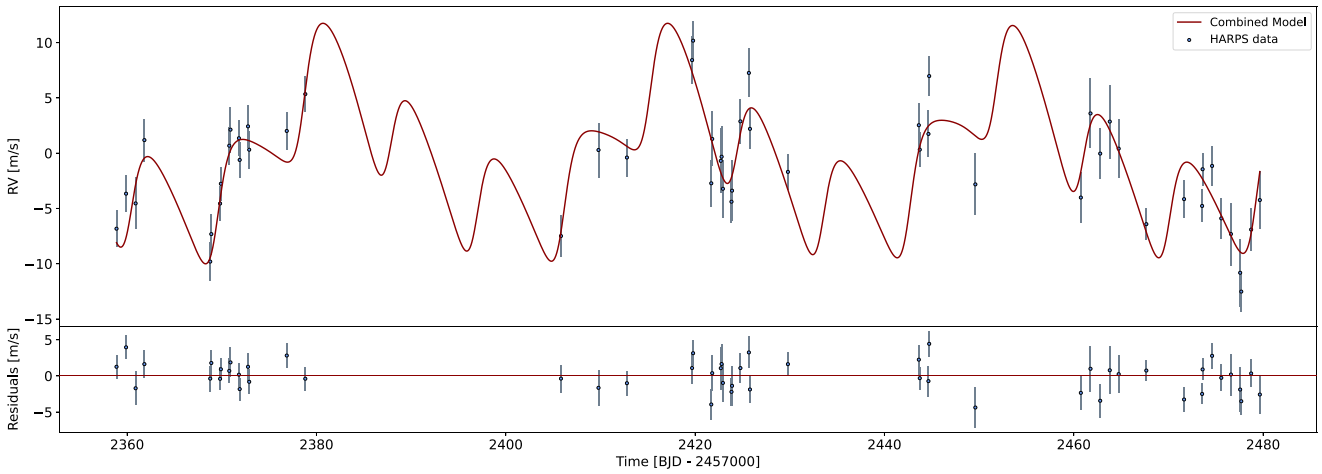

Figure 5. The full RV HARPS timeseries showing the combined best fit model from planets b and c in red. Residuals after subtracting the model are shown further.

find the ionization and excitation equilibrium to converge on the best set of spectroscopic parameters. This process makes use of a grid of Kurucz model atmospheres (Kurucz 1993) and the radiative transfer code MOOG (Sneden 1973). We also derived a more accurate trigonometric surface gravity using recent *Gaia* data following the same procedure as described in Sousa et al. (2021) which provided a consistent value when compared with the spectroscopic surface gravity. The resulting spectroscopic parameters are given in Table 1. The derived temperature of 6146 ± 62 K is indicative of a late F star as opposed to the G0 type specified in the literature (Houk & Cowley 1975), but not different at high enough confidence for us to reclassify the spectral type.

The abundances of the following elements were also derived using the same tools and models as for the stellar spectroscopic parameters: Mg, Al, Ti, Si, and Ni (detailed in e.g. Adibekyan et al. 2012, 2015), neutron capture elements (used later to obtain ages) as explained in Delgado Mena et al. (2017), and C and O (following Bertran de Lis et al. 2015; Delgado Mena et al. 2021). Although the EWs of the spectral lines were automatically measured with ARES, we performed careful visual inspection of the EWs measurements.

3.2 Stellar mass, radius, and age

The stellar mass, radius, and age were estimated from the spectroscopically derived parameters using the PARAM 1.3 web-interface[2] (da Silva et al. 2006), leading to $R_\star = 1.264 \pm 0.033\,R_\odot$, $M_\star = 1.204 \pm 0.025\,M_\odot$, and Age $=2.3 \pm 1.0$ Gyr. As an alternative we also estimated the stellar mass from the PARAM 1.3 values using the calibration presented in Torres, Andersen & Giménez (2010a) which provided a consistent result ($M_{\star,\,\mathrm{Torres}} = 1.19 \pm 0.03\,M_\odot$).

As an independent determination of the basic stellar parameters, we also performed an analysis of the broad-band spectral energy distribution (SED) of the star together with the *Gaia* EDR3 parallax (with no systematic offset applied; see, e.g. Stassun & Torres 2021), in order to determine an empirical measurement of the stellar radius, following the procedures described in Stassun & Torres (2016); Stassun, Collins & Gaudi (2017); Stassun et al. (2018). We pulled the $B_T V_T$ magnitudes from *Tycho-2*, the JHK_S magnitudes from *2MASS*, the W1–W4 magnitudes from *WISE*, and the $GG_{\mathrm{BP}}G_{\mathrm{RP}}$ magnitudes from *Gaia*. Together, the available photometry spans the stellar SED over the wavelength range 0.4–22 μm.

We performed a fit using Kurucz stellar atmosphere models, with the main parameters being the effective temperature (T_{eff}), surface gravity ($\log g$), and metallicity ([Fe/H]), for which we adopted the spectroscopically determined values. The remaining free parameter is the extinction A_V, which we limited to the maximum line-of-sight value from the Galactic dust maps of Schlegel, Finkbeiner & Davis (1998). The resulting fit has a reduced χ^2 of 1.0 and best fit $A_V = 0.04 \pm 0.04$. Integrating the model SED gives the bolometric flux at Earth, $F_{\mathrm{bol}} = 4.123 \pm 0.096 \times 10^{-9}\,\mathrm{erg\,s^{-1}\,cm^{-2}}$. Taking the F_{bol} and T_{eff} together with the *Gaia* parallax, gives the stellar radius, $R_\star = 1.293 \pm 0.030\,\mathrm{R}_\odot$. In addition, we can again estimate the stellar mass from the empirical relations of Torres, Andersen & Giménez (2010b), giving $M_\star = 1.20 \pm 0.07\,\mathrm{M}_\odot$.

All of our methods of stellar parameter estimation produce consistent results. We adopt the PARAM 1.3 values going forwards, and these are listed in Table 1.

3.3 Rotational period and age

Our PARAM fit led to an estimated isochrone age of $=2.3 \pm 1.0$ Gyr. We are also able to estimate the stellar age via the chemical clocks method (see Delgado Mena et al. 2019). The ages estimated from different chemical clocks (together with the Teff and [Fe/H]) are listed in Table 2, giving a weighted average of 1.9 ± 0.3 Gyr consistent with the PARAM age. This small error bar just reflects the good agreement between the ages obtained from different chemical clocks. We conservatively adopt the PARAM age with its larger error bar, given the uncertainties associated with stellar age estimation.

We do not find any evidence of periodic variability indicative of rotation in the *TESS* light curves.

Through the FWHM of the HARPS spectra CCF we are able to estimate the projected rotation velocity $v \sin i$ for the star. The mean FWHM across the spectra is $9.12\,\mathrm{km\,s^{-1}}$. Using a calibration similar to the one presented in Santos et al. (2002); Maldonado et al. (2017); Hojjatpanah et al. (2019, and references therein) this FWHM implies a $v \sin i$ of $5.63 \pm 0.5\,\mathrm{km\,s^{-1}}$. We also re-derived the $v \sin i$ by performing spectral synthesis with MOOG on 36 isolated iron lines and by fixing all the stellar parameters, macroturbulent velocity, and

[2]http://stev.oapd.inaf.it/cgi-bin/param_1.3

Table 1. Stellar parameters.

Parameter	Value	Source
Identifying information		
Identifier	HD 212 729	
TOI	TOI-1052	*TESS*
TIC ID	317 060 587	*TESS*
2MASS ID	22300272–7538476	2MASS
Gaia ID 6357524189130820992		*Gaia* DR3
Astrometric parameters		
RA (J2000, deg)	337.51023851341	*Gaia* DR3
Dec. (J2000, deg)	−75.64656089247	*Gaia* DR3
Parallax (mas)	7.74 ± 0.01	*Gaia* DR3
Distance (pc)	128.7 ± 0.2	*Gaia* DR3
Photometric parameters		
B	10.09 ± 0.04	Tycho
V	9.51 ± 0.02	Tycho
T	9.02 ± 0.01	*TESS*
G	9.40 ± 0.01	*Gaia* DR3
J	8.56 ± 0.02	2MASS
H	8.25 ± 0.04	2MASS
K	8.25 ± 0.03	2MASS
W1	8.160 ± 0.023	WISE
W2	8.255 ± 0.021	WISE
W3	8.190 ± 0.020	WISE
W4	8.119 ± 0.174	WISE
Abundances		
[Fe/H](dex)	0.140 ± 0.013	Section 3
[MgI/H](dex)	0.08 ± 0.04	Section 3
[AlI/H](dex)	0.10 ± 0.02	Section 3
[SiI/H](dex)	0.11 ± 0.04	Section 3
[TiI/H](dex)	0.12 ± 0.03	Section 3
[NiI/H](dex)	0.13 ± 0.03	Section 3
Bulk parameters		
Mass ($M_\odot$)	1.204 ± 0.025	Section 3 (PARAM)
Radius ($R_\odot$)	1.264 ± 0.033	Section 3 (PARAM)
$T_{\rm eff}$ (K)	6146 ± 62	Section 3
log g (cm s^{-2})	4.30 ± 0.02	Section 3 (*Gaia*)
log g (cm s^{-2})	4.39 ± 0.11	Section 3 (spec)
$v_{\rm mic}$ (km s^{-1})	1.28 ± 0.02	Section 3
$v \sin i$ (km s^{-1})	5.0 ± 0.9	Section 3
$P_{rot}/\sin i$ (d)	12.8 ± 2.3	Section 3
Age(Gyrs)	2.3 ± 1.0	Section 3 (PARAM)
mean $log(R'_{HK})$	−5.32 ± 0.02	HARPS

Note: sources: *TESS* (Stassun et al. 2019); 2MASS (Skrutskie et al. 2006); Tycho (Høg et al. 2000); WISE (Wright et al. 2010); and *Gaia* (Gaia Collaboration et al. 2016, 2022)

Table 2. Chemical clock age estimates (see Delgado Mena et al. 2019, Table 10).

Clock	Value (Gyr)
[Y/Zn]	2.1 ± 0.5
[Y/Ti]	1.6 ± 0.7
[Y/Mg]	1.4 ± 0.6
[Sr/Ti]	2.3 ± 1.3
[Sr/Mg]	2.0 ± 1.1
[Y/Si]	1.6 ± 0.7
[Sr/Si]	1.8 ± 1.2
[Y/Al]	2.7 ± 0.3
Weighted mean	1.9 ± 0.3

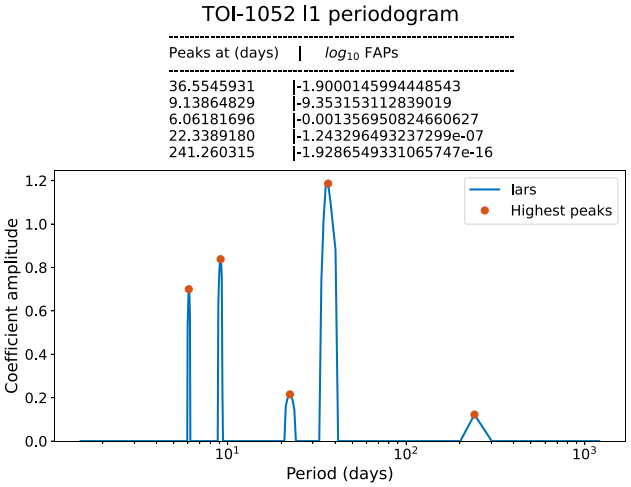

Figure 6. l_1 Periodogram as discussed in Section 3.4 showing significant peaks at 9.14 and 36.6 d. Peak values and false alarm probabilities (FAPs) are shown above in the periodogram.

limb-darkening coefficient (Costa Silva, Delgado Mena & Tsantaki 2020), leading to a consistent value of $v \sin i = 5.0 \pm 0.9$ km s^{-1}, which we adopt. The linear limb-darkening coefficient (0.7) was determined using the ExoCTK package (Bourque et al. 2021) using the determined stellar parameters. The macroturbulent velocity (4.4 km s^{-1}) was determined using the temperature and gravity dependent empirical formula from Doyle et al. (2014).

We estimated the (projected) rotation period directly via the spectroscopic $v \sin i$ and the $R_\star$ determined earlier, which gives $P_{\rm rot}/\sin i = 12.8 \pm 2.3$ d. Assuming the stellar orbital inclination is $i \approx 90°$, then this would represent approximately the true rotation period.

3.4 Signal identification

We computed the l_1 periodogram (e.g. Hara et al. 2017, 2020) to find periodicities in the RV data. The l_1 periodogram uses the theory of compressed sensing adapted for handling correlated noise to analyse the RV without the estimation of the frequency iteratively, see Hara et al. (2017, 2020) for more information. A fundamental difference of the l_1 periodogram over the typically used Lomb–Scargle (Lomb 1976; Scargle 1982; VanderPlas 2018) is that all possible frequencies are tested simultaneously. This method reduces aliases in the periodogram. Fig. 6 shows two significant signals, considering the model noise with a 1.5 m s^{-1} jitter noise, consistent with the eventual jitter found by our best fit model in Table 4. Both the 9.14-d transiting planet period and an additional 36.6-d period were found to be significant with a False Alarm Probability (FAP) < 1.0 *percent* for the 9.14 d and 1.2 per cent for the 36.6 d, as opposed to the other shown peaks which have FAP > 99 per cent. Lomb–Scargle periodograms of the RVs with and without the planet signals, FWHM, bisector span (BIS), log RHK, and CCF contrast, calculated with `astropy` (Astropy Collaboration et al. 2022), are shown in Fig. 7, to investigate the planet peaks further and consider a potential activity source for the significant signals. No significant power is found at the 9-d or 36-d periods in any of the indicators. Fig. 7 also demonstrates that two periodic components are required to model the RVs, with no further periodic signals found once the two planets are removed. Note the the initially most significant peak seen in the RVs in the Lomb–Scargle periodogram is at 22 d, which

Table 3. Prior distributions used in our joint fit model, fully described in Section 4. The priors are created using distributions in `PyMC3` with the relevant inputs to each distribution described in the table footer. Fit results and derived parameters can be found in Table 4.

Parameter	(unit)	Prior distribution
Planet b		
Period P_b	(days)	$\mathcal{N}(9.13966, 0.001)$
Ephemeris $t_{0,\,b}$	(BJD-2457000)	$\mathcal{N}(1332.9448, 0.02)$
Radius log (R_b)	(log $R_\odot$)	$\mathcal{N}(-3.733^*, 1.0)$
Impact parameter b_b		$\mathcal{U}(0, 1 + R_b/R_*)$
$e_b \sin\omega_b$		$\mathcal{U}$(Unit disc)
$e_b \cos\omega_b$		$\mathcal{U}$(Unit disc)
K_b	($m\,s^{-1}$)	$\mathcal{U}(0.0, 50.0)$
Planet c		
Period P_c	(days)	$\mathcal{N}(35.97306, 4.0)$
Ephemeris $t_{0,\,c}$	(BJD-2457000)	$\mathcal{N}(2423.3168, 20.0)$
$e_c \sin\omega_c$		$\mathcal{U}$(Unit disc)
$e_c \cos\omega_c$		$\mathcal{U}$(Unit disc)
K_c	($m\,s^{-1}$)	$\mathcal{U}(0.0, 50.0)$
Star		
Mass M_*	($M_\odot$)	$\mathcal{N}_\mathcal{B}(1.204, 0.025, 0.0, 3.0)$
Radius R_*	($R_\odot$)	$\mathcal{N}_\mathcal{B}(1.264, 0.033, 0.0, 3.0)$
Photometry		
TESS mean		$\mathcal{N}(0.0, 1.0)$
log (Jitter)	($m\,s^{-1}$)	$\mathcal{N}(-7.40^\dagger, 10)$
HARPS RVs		
Offset	($m\,s^{-1}$)	$\mathcal{N}(54945.0, 10.0)$
log (Jitter)	($m\,s^{-1}$)	$\mathcal{N}(0.37^\dagger, 5.0)$

*Notes.*Distributions:
$\mathcal{N}(\mu, \sigma)$: a normal distribution with a mean μ and a standard deviation σ;
$\mathcal{N}_\mathcal{B}(\mu, \sigma, a, b)$: a bounded normal distribution with a mean μ, a standard deviation σ, a lower bound a, and an upper bound b (bounds optional);
$\mathcal{U}(a, b)$: a uniform distribution with a lower bound a, and an upper bound b.
Prior values:
* equivalent to $0.5(\log(D)) + \log(R_*)$ where D is the transit depth (ppm multiplied by 10^{-6}) and R_* is the mean of the prior on the stellar radius ($R_\odot$);
† equivalent to the log of the minimum error on the HARPS data ($m\,s^{-1}$), or the mean error on the *TESS* data. We fit a log value to enforce an broad, non-zero prior covering several orders of magnitude.

is seen with low significance in the l_1 periodogram. The 22-d peak is an artefact arising from both the 9.14-d and 36-d planet peaks and vanishes when both planets are removed. Similarly, the 6-d signal seen in both periodograms is an artefact of the planet b peak.

Given the robust detection of the transiting planet in the radial velocities, we are able to confirm the known planetary candidate as TOI-1052 b. Given that there is no sign of stellar activity in any indicator at the 36.6-d additional period, and this period does not match the estimated stellar rotation period or its harmonics, we claim this as an additional planet in the system, TOI-1052 c. The joint fit of photometry and spectroscopy in Section 4 finds a period for planet c of $35.81^{+0.45}_{-0.38}$d. TOI-1052 c is just within the 4:1 resonance of planet b. The system dynamics are discussed in Section 5.1.

4 JOINT MODELLING

The photometry from *TESS* and spectroscopy from HARPS were combined in a joint fit using the `exoplanet` (Foreman-Mackey et al. 2021) code framework. This package also makes use of `starry` (Luger et al. 2019) and `PYMC3` (Salvatier, Wieckiâ & Fonnesbeck 2016). The photometric model is adjusted to account for the *TESS* exposure time of 2 min.

The model constructs two Keplerian orbits, one for each planet, with orbital period P, epoch t_0, impact parameter b, eccentricity e and angle of periastron ω as free parameters determining the orbit. The orbital period and epoch are drawn from Gaussian prior distributions with a mean drawn from initial fits and a standard deviation of 0.001 and 4 d for planets b and c, respectively, approximately 10 times larger than the eventual errors on those parameters. The impact parameter is drawn uniformly between 0 and $1 + R_p/R_\star$, where R_p is the planetary radius. e and ω are drawn via sampling $e\sin\omega$ and $e\cos\omega$ from a unit disc distribution then deriving e and ω. Additionally the stellar mass and radius are allowed to vary in a Gaussian distribution according to their values from Section 3.

Once the orbit is defined, the planet to star radius ratio $R_p/R_\star$ and RV semi-amplitude K are drawn from wide uniform distributions. Limb darkening parameters are drawn from the quadratic limb darkening parametrization of Kipping (2013). We introduce a systematic RV offset, a *TESS* photometry offset, and instrumental jitter parameters for both instruments as extra parameters. Jitter is drawn from a broad Gaussian distribution in log-space to allow for a wide range of orders of magnitude, and is then added to the measured instrumental noise in quadrature All model priors are detailed in Table 3.

We do not include a model for the stellar noise, apart from the jitter term in the RVs, as no significant periodic signal was found in either the RVs, stellar activity indicators or photometry aside from the two planetary signals.

We use a No U-Turn Sampler (NUTS) variant of the Hamiltonian Monte Carlo (HMC) algorithm to draw samples from the posterior chain, for which we use 12 chains each with 5000 steps for a total of 60 000 iterations. We treat the first 1500 samples drawn from each chain as burn-in and subsequently discard them. The resulting Gelman–Rubin statistics (Brooks & Gelman 1998) for each variable are $<<1.05$, demonstrating the chains have converged.

Our initial fits revealed a marginally significant eccentricity for both planets (at 2.5σ for planet b and 2.9σ for planet c). We present fit posterior values with eccentricity, and with both planets fixed at zero eccentricity, in Table 4. The resulting planet parameters are consistent in both models. To compare the models we calculate the WAIC (widely applicable information criterion), which estimates the expected log pointwise predictive density (elpd) of the models (for details on the criterion see Watanabe 2010; Vehtari, Gelman & Gabry 2017). The eccentric model is slightly favoured with a higher elpd, with a difference of 4.0, although this difference is not large enough to be considered significant. We adopt the free eccentricity results going forwards.

Through the results of this analysis, we determine that TOI-1052 b is a mini-Neptune of radius $2.87^{+0.29}_{-0.24}\,R_\oplus$ and mass $16.9 \pm 1.7\,M_\oplus$. From these values we infer a bulk density of $3.9^{+1.7}_{-1.3}\,g\,cm^{-3}$. The non-transiting planet TOI-1052 c is found to have $M \sin i_c = 34.3^{+4.1}_{-3.7}\,M_\oplus$. No evidence of transits is seen for planet c. Fig. 10 shows the two planets in the context of the exoplanet population.

The near 4:1 ratio of the orbital periods, and potential eccentricity, invite questions as to whether there is a third planet in between planets b and c, forming a 1:2:4 ratio. Two planets may mimic a single planet with an eccentric orbit in RV observations, although TOI-1052 c is below the 3σ significant eccentricity criterion for this issue found in Wittenmyer et al. (2019). We could not find any evidence of such a

Table 4. TOI-1052 fit and derived parameters: median and 68 per cent confidence interval.

Model		With eccentricity (adopted)		Fixed eccentricity	
System parameters:					
$u_{1,\,TESS}$		$0.80^{+0.61}_{-0.55}$		$0.85^{+0.59}_{-0.57}$	
$u_{2,\,TESS}$		$-0.07^{+0.52}_{-0.49}$		$-0.12^{+0.54}_{-0.48}$	
$TESS_{\rm offset}$	ppm	$-7.9^{+3.3}_{-3.3}$		$-7.9^{+3.2}_{-3.2}$	
σ_{TESS}	ppm	$61.0^{+2.3}_{-2.3}$		$61.0^{+2.3}_{-2.3}$	
σ_{HARPS}	m s^{-1}	$0.79^{+0.61}_{-0.65}$		$1.62^{+0.42}_{-0.42}$	
Systemic RV	m s^{-1}	$54946.02^{+0.38}_{-0.39}$		$54945.75^{+0.38}_{-0.39}$	
Planetary parameters:		b	c	b	c
P	days	$9.139703^{+0.000190}_{-0.000197}$	$35.806^{+0.453}_{-0.381}$	$9.139664^{+0.000191}_{-0.000209}$	$35.779^{+0.466}_{-0.420}$
T_0	BJD − 2457000	$1332.9442^{+0.0057}_{-0.0055}$	$2425.13^{+1.63}_{-1.64}$	$1332.9454^{+0.0060}_{-0.0056}$	$2427.46^{+0.54}_{-0.50}$
K	m s^{-1}	$4.70^{+0.46}_{-0.46}$	$6.11^{+0.80}_{-0.69}$	$4.45^{+0.54}_{-0.52}$	$5.33^{+0.62}_{-0.63}$
e		$0.180^{+0.090}_{-0.071}$	$0.237^{+0.090}_{-0.082}$	0 (fixed)	0 (fixed)
ω	rad	$-2.07^{+0.24}_{-0.42}$	$-0.79^{+0.47}_{-0.53}$	-	–
$a/R_\star$		$15.51^{+0.43}_{-0.41}$	38.6 ± 1.1	$15.53^{+0.43}_{-0.41}$	38.6 ± 1.1
i	deg	$87.53^{+0.24}_{-0.20}$	–	$87.55^{+0.46}_{-0.29}$	–
$R_p/R_\star$		$0.0194^{+0.0018}_{-0.0015}$	–	$0.0184^{+0.0013}_{-0.0014}$	–
b		$0.808^{+0.052}_{-0.079}$	–	$0.727^{+0.052}_{-0.085}$	–
Derived parameters:		b	c	b	c
M_p	$M_\oplus$	$16.9^{+1.7}_{-1.7}$	–	$16.4^{+2.0}_{-1.9}$	–
R_p	$R_\oplus$	$2.87^{+0.29}_{-0.24}$	–	$2.72^{+0.22}_{-0.22}$	–
ρ_p	g cm^{-3}	$3.93^{+1.7}_{-1.3}$	–	$4.48^{+2.0}_{-1.4}$	–
a_p	au	$0.09103^{+0.00062}_{-0.00063}$	$0.2263^{+0.0024}_{-0.0023}$	0.09102 ± 0.00062	0.2261 ± 0.0024
S	$S_\oplus$	246 ± 13	$39.7^{+2.3}_{-2.2}$	245^{+14}_{-13}	$39.7^{+2.3}_{-2.2}$
T_{eq}†	K	1135	719	1134	719
$M_P \sin i$	$M_\oplus$	–	$34.3^{+4.1}_{-3.7}$	–	$30.9^{+3.6}_{-3.7}$

Notes.∗ For TOI 1052c T_0 corresponds to the time when the planet would have transited.
†Assuming a Bond Albedo of 0.3.

hidden planet, which might be expected to show in the RV residuals if the model is forced to be circular. Absent that evidence, we proceed with the two-planet model but note this possibility in case future observations can probe the system further.

5 DISCUSSION

5.1 Dynamical analysis

The wide range of allowed eccentricities for both planets raise questions as to their stability and dynamical interactions. Further, the approximate 4:1 ratio of the planets' orbital periods invites a more detailed analysis of a potential resonant interaction and how it affects the stability of the system.

First, because this system is a two-planet system, we can determine if it is Hill stable analytically. By using the procedure outlined in Veras et al. (2013), which is based on the equations in Donnison (2006, 2011), we find that the TOI-1052 is Hill stable for all planetary eccentricities in the ranges $e_{\rm b} = 0.0 - 0.3$ and $e_{\rm c} = 0.0 - 0.3$. In fact, the system is comfortably Hill stable: even in the scenario where $e_{\rm b} = e_{\rm c} = 0.3$, the system would be Hill stable for $a_{\rm c}/a_{\rm b} \gtrsim 2.12$, whereas actually $a_{\rm c}/a_{\rm b} \approx 2.49$.

Hence, residence in a strong mean-motion resonance is not necessarily required to stabilize the system. Nevertheless, the system's proximity to a strong mean-motion resonance is of interest, particularly in context of the entire exoplanet population. Fig. 5 of Weiss et al. (2022) illustrates a statistically significant asymmetry in the population of two-planet pairs which reside just interior versus just exterior to the strongest (first-order) mean-motion resonances, first noted in Fabrycky et al. (2014). The observed population of 4:1 planetary pairs might not yet be high enough for a 4:1 asymmetry to be detectable. In this respect, the TOI-1052 system might provide a valuable data point, although it cannot be excluded that another planet lies between the two detected planets.

In order to explore the system's proximity to resonance, we employ the semi-analytic libration width prescription of Gallardo, Beaugé & Giuppone (2021). This prescription effectively computes bounds within which mean-motion resonant behaviour is possible through a numerical procedure mixed in with analytical theory.

We plot the libration width curves for four cases ($e_{\rm b} = 0.0$, 0.1, 0.2, 0.3) in Fig. 11 by using an eccentricity resolution of 0.025 in the numerical integration. Superimposed are the uncertainties for the current location of TOI-1052 c. Comparing these uncertainties with the libration width locations indicates that the TOI-1052 system is definitely not in resonance (at least a third-, second-, or first-order resonance), and resides just interior to the 4:1 resonance.

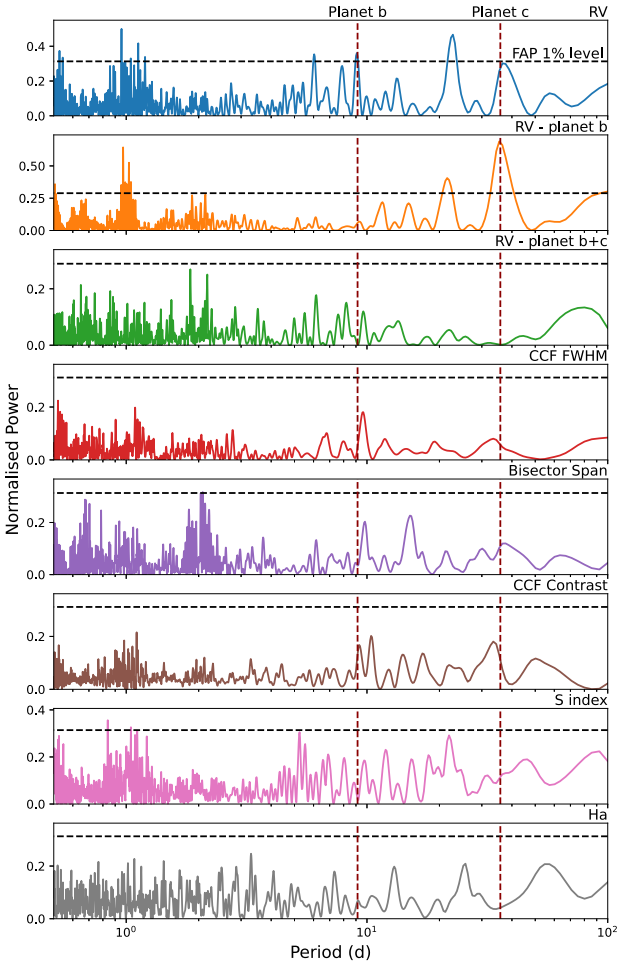

Figure 7. Lomb–Scargle periodogram of HARPS RVs and activity indicators. The orbital period of each planet is shown as vertical dashed lines. Horizontal dashed lines show the FAP 1 per cent level. A 22-d artefact is seen in the raw RVs at the top, but vanishes when both planet models are removed.

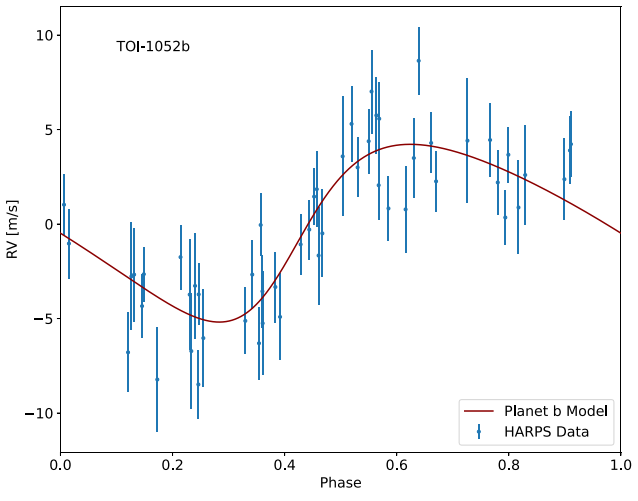

Figure 8. Radial velocities phase-folded at the best-fitting period of TOI-1052 b, with best fit model overplotted in red.

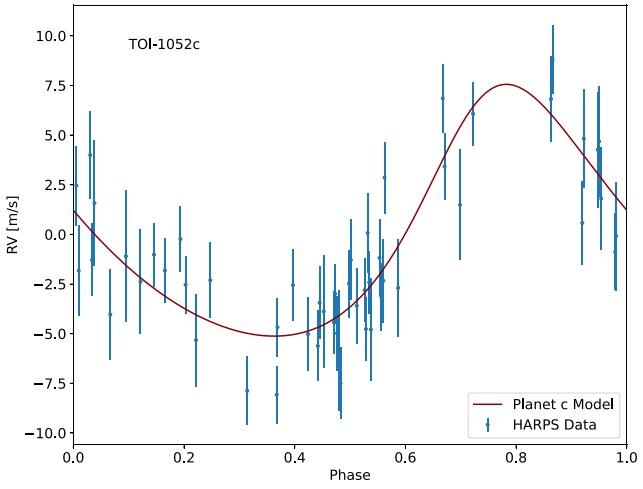

Figure 9. Radial velocities phase-folded at the best-fitting period of TOI-1052 c, with best fit model overplotted in red.

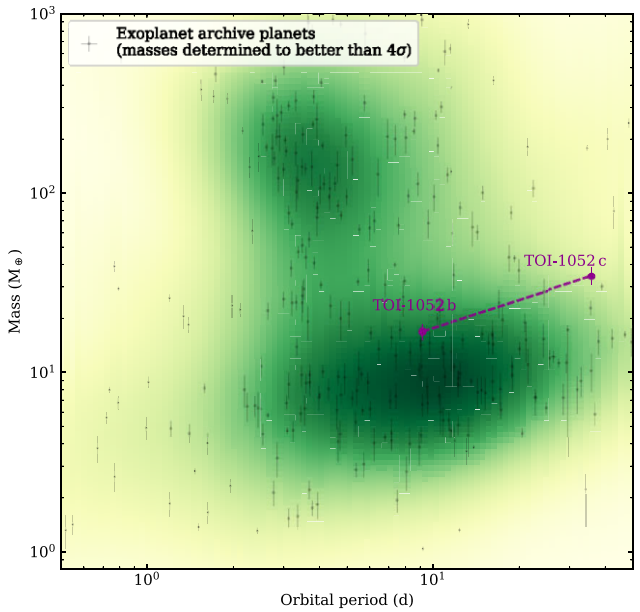

Figure 10. Period-Mass diagram showing both planets, with TOI-1052c plotted at its $M_P \sin i$ value. The background density distribution of known exoplanets is shown in green.

The system's close proximity to resonance is characteristic of many exoplanetary systems, although the proximity to a relatively high-order resonance is noteworthy. Proximity to resonance can be a marker for the differential migration rates of planets in their nascent protoplanetary disc, although to date this has primarily been investigated in depth for first-order resonances (Huang & Ormel 2023).

5.2 Internal structure

TOI-1052 b is similar to Uranus or Neptune in mass, but has a considerably smaller radius and therefore a denser interior. Fig. 12,

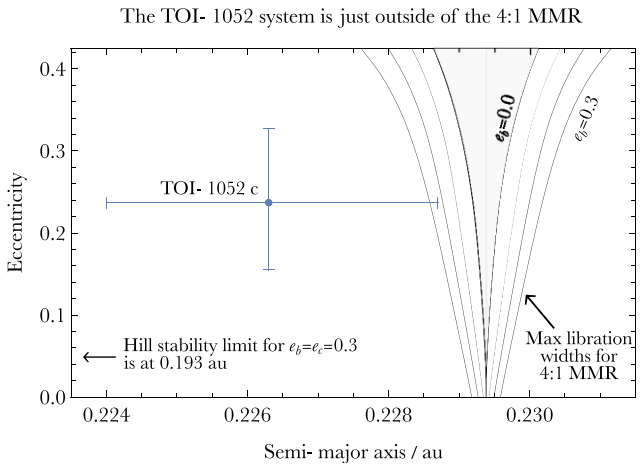

Figure 11. Proximity of the two planets in the TOI-1052 to the 4:1 mean-motion resonance. The four pairs of curves are libration widths for this resonance. These curves, moving outwards, correspond to $e_b = 0.0, 0.1, 0.2, 0.3$. The planet TOI-1052 c is nearly outside all of these curves, adding to the asymmetry seen around mean-motion commensurabilities in the exoplanet population. This system is also Hill stable, with the critical limit off the scale of the plot.

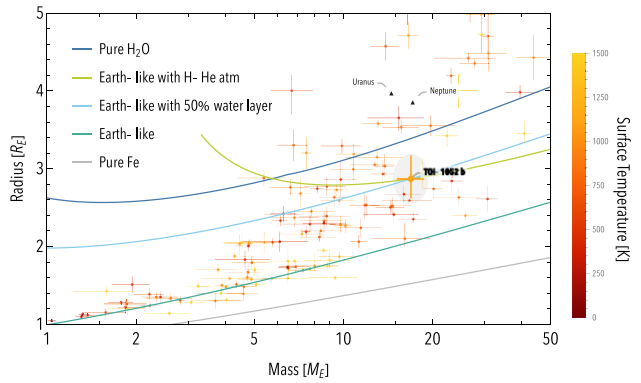

Figure 12. Mass–radius diagram showing various internal structure lines from our model labelled in the legend. TOI-1052b can be explained by an Earth-like composition with either 50 per cent water or a H-He atmosphere as described in the text.

which shows the Mass–Radius relation, demonstrates that TOI-1052 b is located between the water line and Earth-like compositional line, suggesting a significant fraction of refractory materials. In comparison, both Uranus and Neptune are located above the pure-water line.

For TOI-1052b, two limiting cases come to mind: a planet with a rocky interior and a substantial hydrosphere and a refractory-rich planet with a primordial H-He atmosphere. We investigate these two scenarios with a layered interior model, consisting of up to four layers: a H-He atmosphere, a water layer, a silicate mantle, and an iron core (see Dorn et al. 2017). Using the inferred age and elemental abundances of TOI-1052, we solve the standard structure equations for two models: 1.) a model where we assume that TOI-1052 b contains no water (*no-water model*) and 2.) a model where we conversely assume that TOI-1052 b contains no H-He atmosphere (*no-atmosphere model*). We put no constraints on the compositions, that is, the elemental ratios, of the other layers. As a result, the iron-to-rock ratio can take any value. For both models, we apply a nested sampling algorithm (Buchner et al. 2014) to explore the permitted parameter ranges that reproduce the measured masses and radii of TOI-1052 b.

We find that the no-water model favours a core-to-mantle mass fraction of nearly unity: 0.96 ± 0.17 with a H-He envelope of $2^{+1.4}_{-0.8}$ %. In the case of the no-atmosphere model, while the core-to-mantle mass fraction is poorly constrained (0.6 ± 0.5), this model predicts a water mass fraction of 0.43 ± 0.12. The larger uncertainties are caused by the wide range of possible core, mantle, and water layer masses that can reproduce the observed radius and mass compared to the no-water model. Assuming a fixed iron-to-rock ratio, for example, similar to the host star's elemental ratios, decreases the model's uncertainty significantly.

We note that at high planetary masses, layers might not be as distinct as assumed here (e.g. Helled & Stevenson 2017; Bodenheimer et al. 2018). Moreover, the atmospheric mass fraction may be underestimated due to pollution of the H-He envelope by heavier elements, leading to further contraction of the atmosphere (Lozovsky et al. 2018). The interior model also neglects any water that is dissolved deep in the interior, which could increase the overall water mass fraction (Dorn & Lichtenberg 2021). Nevertheless, while these details could change the exact values inferred here, it is clear that TOI-1052 b is enriched with refractory materials and any H-He atmosphere is likely to be minimal.

Additionally, the planet's elemental abundances could differ from its host star, which can change the mantle and the temperature structure. We therefore also considered structure models with varying elemental abundances to investigate this effect. We find that the inferred possible compositions and their error for TOI-1052 b do not change significantly.

6 CONCLUSIONS

We report the discovery and characterization of two new planets just outside the 4:1 mean-motion resonance in the bright, V = 9.5 TOI-1052 system, using *TESS* mission data and HARPS RV measurements. We used high-resolution imaging from the Zorro speckle imaging instrument in order to investigate the presence of any nearby companions and find none within the detector limits. We estimated the projected stellar rotation period to be around 12.8 d from measuring line broadening in the spectra, and derived stellar parameters, chemical abundances and an age estimate to reveal the system in more detail.

TOI-1052b is a Neptune-mass planet with a sub-Neptune radius, with a potentially eccentric 9.13-d orbit. The planet's density of $3.93^{+1.7}_{-1.3}$ g cm^{-3} implies a composition denser with more heavy elements than Neptune. Limiting case layered interior models show a degeneracy between a rocky planet with a 2 per cent H-He atmosphere and a water-rich planet with a water mass fraction of 0.43.

The companion planet TOI-1052c shows an $M_P \sin i$ of $34.3^{+4.1}_{-3.7} M_\oplus$, approx. double the mass of planet b, and orbits on a 35.8-d period. Given its presence near the 4:1 mean-motion resonance, and the potential eccentricity of both planets, the system provides an interesting case study for dynamical interactions.

ACKNOWLEDGEMENTS

Based on observations collected at the La Silla Observatory, ESO (Chile), with the HARPS spectrograph at the 3.6-m telescope for programs 1102.*C* − 0249(*F*), 106.21*TJ*.001, and 105.20*G*9.001.

DJA is supported by UKRI through the STFC (ST/R00384X/1) and EPSRC (EP/X027562/1). AO and FH are funded by an STFC studentship. Co-funded by the European Union (ERC, FIERCE, 101052347). Views and opinions expressed are however those of the authors only and do not necessarily reflect those of the European Union or the European Research Council. Neither the European Union nor the granting authority can be held responsible for them. This work was supported by FCT – Fundação para a Ciência e a Tecnologia through national funds and by FEDER through COMPETE2020 – Programa Operacional Competitividade e Internacionalização by these grants: UIDB/04434/2020; UIDP/04434/2020. VA acknowledges the support from FCT through the following grant number: 2022.06962.PTDC. SGS acknowledges the support from FCT through Investigador FCT contract nr. CEECIND/00826/2018 and POPH/FSE (EC). EDM acknowledges the support from FCT through Investigador FCT contract nr. 2021.01294.CEECIND. HK and RH carried out this work within the framework of the NCCR PlanetS supported by the Swiss National Science Foundation under grants 51NF40_182901 and 51NF40_205606. CD acknowledges support from the Swiss National Science Foundation under grant number PZ00P2_174028. This project has received funding from the European Research Council (ERC) under the European Union's Horizon 2020 research and innovation programme (grant agreement SCORE Number 851555). JLB is partly funded by grants LCF/BQ/PI20/11760023, Ramón y Cajal fellowship with code RYC2021-031640-I, and the Spanish MCIN/AEI/10.13039/501100011033 grant number PID2019-107061GB-C61. SH acknowledges CNES funding through the grant number 837319.

This work made use of `tpfplotter` by J. Lillo-Box (publicly available in www.github.com/jlillo/tpfplotter), which also made use of the python packages `astropy`, `lightkurve`, `matplotlib`, and `numpy`.

Funding for the *TESS* mission is provided by NASA's Science Mission Directorate. We acknowledge the use of public *TESS* data from pipelines at the *TESS* Science Office and at the *TESS* Science Processing Operations Centre. Resources supporting this work were provided by the NASA High-End Computing (HEC) Program through the NASA Advanced Supercomputing (NAS) Division at Ames Research Centre for the production of the SPOC data products. This research has made use of the Exoplanet Follow-up Observation Program website, which is operated by the California Institute of Technology, under contract with the National Aeronautics and Space Administration under the Exoplanet Exploration Program.

Some of the observations in this paper made use of the High-Resolution Imaging instrument Zorro and were obtained under Gemini LLP Proposal Number: GN/S-2021A-LP-105. Zorro was funded by the NASA Exoplanet Exploration Program and built at the NASA Ames Research Centre by Steve B. Howell, Nic Scott, Elliott P. Horch, and Emmett Quigley. Zorro was mounted on the Gemini South telescope of the international Gemini Observatory, a program of NSF's OIR Lab, which is managed by the Association of Universities for Research in Astronomy (AURA) under a cooperative agreement with the National Science Foundation on behalf of the Gemini partnership: the National Science Foundation (United States), National Research Council (Canada), Agencia Nacional de Investigación y Desarrollo (Chile), Ministerio de Ciencia, Tecnología e Innovación (Argentina), Ministério da Ciência, Tecnologia, Inovações e Comunicações (Brazil), and Korea Astronomy and Space Science Institute (Republic of Korea).

This work has made use of data from the European Space Agency (ESA) mission *Gaia* (https://www.cosmos.esa.int/gaia), processed by the *Gaia* Data Processing and Analysis Consortium (DPAC, https://www.cosmos.esa.int/web/gaia/dpac/consortium). Funding for the DPAC has been provided by national institutions, in particular the institutions participating in the *Gaia* Multilateral Agreement.

7 DATA AVAILABILITY

TESS data are accessible via the MAST (Mikulski Archive for Space Telescopes) portal at https://mast.stsci.edu/portal/Mashup/Clients/Mast/Portal.html. Imaging data from Zorro are accessible via the ExoFOP-*TESS* archive at https://exofop.ipac.caltech.edu/tess/target.php?id = 317060587. The exoplanet modelling code and associated python scripts for parameter analysis and plotting are available upon reasonable request to the author. RV data are presented in Table A1.

REFERENCES

Adibekyan V. Z., Sousa S. G., Santos N. C., Delgado Mena E., González Hernández J. I., Israelian G., Mayor M., Khachatryan G., 2012, A&A, 545, 32
Adibekyan V., et al., 2015, A&A, 583, 94
Akeson R. L., et al., 2013, PASP, 125, 989
Alibert Y., Mordasini C., Benz W., Naef D., 2010, in Goździewski K., Niedzielski A., Schneider J.eds, EAS Publications SeriesVol. 42, EAS Publications Series, p. 209 , Available at https://www.eas-journal.org/articles/eas/abs/2010/03/eas1042024/eas1042024.html
Alibert Y., Thiabaud A., Marboeuf U., Swoboda D., Benz W., Mezger K., Leya i., 2015, in AAS/Division for Extreme Solar Systems Abstracts, 47, 115.02
Aller A., Lillo-Box J., Jones D., Miranda L. F., Barceló Forteza S., 2020, A&A, 635, 128
Armstrong D. J., et al., 2020, Nature, 583, 39
Astropy Collaboration et al., 2022, ApJ, 935, L167
Baranne A., et al., 1996, A&AS, 119, 373
Beaugé C., Nesvorný D., 2013, ApJ, 763, L12
Bertran de Lis S., Delgado Mena E., Adibekyan V. Z., Santos N. C., Sousa S. G., 2015, A&A, 576, 89
Bodenheimer P., Stevenson D. J., Lissauer J. J., D'Angelo G., 2018, ApJ, 868, L138
Boué G., Figueira P., Correia A. C. M., Santos N. C., 2012, A&A, 537, 3
Bourque M., et al., 2021, The Exoplanet Characterization Toolkit (ExoCTK), doi: 10.5281/zenodo.4556063
Brooks S. P., Gelman A., 1998, J. Comput. Graph. Statist., 7, 434
Buchner J., et al., 2014, A&A, 564, 125
Costa Silva A. R., Delgado Mena E., Tsantaki M., 2020, A&A, 634, 136
Delgado Mena E., Tsantaki M., Adibekyan V. Z., Sousa S. G., Santos N. C., González Hernández J. I., Israelian G., 2017, A&A, 606, 94
Delgado Mena E., et al., 2019, A&A, 624, 78
Delgado Mena E., Adibekyan V., Santos N. C., Tsantaki M., González Hernández J. I., Sousa S. G., Bertrán de Lis S., 2021, A&A, 655, 99
Donnison J. R., 2006, MNRAS, 369, 1267
Donnison J. R., 2011, MNRAS, 415, 470
Dorn C., Lichtenberg T., 2021, ApJL, 922, L4
Dorn C., Venturini J., Khan A., Heng K., Alibert Y., Helled R., Rivoldini A., Benz W., 2017, A&A, 597, 37
Doyle A. P., Davies G. R., Smalley B., Chaplin W. J., Elsworth Y., 2014, MNRAS, 444, 3592

Fabrycky D. C., et al., 2014, ApJ, 790, L146
Foreman-Mackey D., et al., 2021, JOSS 6 3285
Fouesneau M., et al., 2022, A&A 674 A28
Gaia Collaboration et al., 2016, A&A, 595, 1
Gaia Collaboration et al., 2023, A&A 674 A1
Gallardo T., Beaugé C., Giuppone C. A., 2021, A&A, 646, 148
Guerrero N. M., et al., 2021, ApJS, 254, 39
Hara N. C., Boué G., Laskar J., Correia A. C. M., 2017, MNRAS, 464, 1220
Hara N. C., et al., 2020, A&A, 636, 6
Helled R., Stevenson D., 2017, ApJ, 840, L4
Hippke M., Heller R., 2019, A&A, 623, 39
Høg E., et al., 2000, A&A, 355, 27
Hojjatpanah S., et al., 2019, A&A, 629, 80
Houk N., Cowley A. P., 1975, University of Michigan Catalogue of two-dimensional spectral types for the HD stars. Volume I. Declinations -90_ to -53_f0.Available at https://ui.adsabs.harvard.edu/abs/1975mcts.book...
..H/abstract
Howell S. B., Furlan E., 2022, Frontiers in Astronomy and Space Sciences, 9, 871163
Howell S. B., Everett M. E., Sherry W., Horch E., Ciardi D. R., 2011, AJ, 142, 19
Hoyer S., et al., 2021, MNRAS, 505, 3361
Huang S., Ormel C. W., 2023, MNRAS, 522, 828
Jenkins J. M., 2002, ApJ, 575, L493
Jenkins J. M., et al., 2010a, ApJ, 713, L87
Jenkins J. M., et al., 2010b, in Radziwill N. M., Bridger A.eds, Society of Photo-Optical Instrumentation Engineers (SPIE) Conference SeriesVol. 7740, Software and Cyberinfrastructure for Astronomy. p. 77400D
Jenkins J. M., et al., 2016, in Chiozzi Gianluca and Guzman, Juan C. Software and Cyberinfrastructure for Astronomy IV 9913 99133E
Jenkins J. M., Tenenbaum P., Seader S., Burke C. J., McCauliff S. D., Smith J. C., Twicken J. D., Chandrasekaran H., 2020, Kepler Data Processing Handbook: Transiting Planet Search, Kepler Science Document KSCI-19081-003, id. 9. Edited by Jon M. Jenkins
Kipping D. M., 2013, MNRAS, 435, 2152
Kurucz R. L., 1993, SYNTHE spectrum synthesis programs and line data
Li J., Tenenbaum P., Twicken J. D., Burke C. J., Jenkins J. M., Quintana E. V., Rowe J. F., Seader S. E., 2019, PASP, 131, 024506
Lomb N. R., 1976, Ap&SS, 39, 447
Lozovsky M., Helled R., Dorn C., Venturini J., 2018, ApJ, 866, L49
Luger R., Agol E., Foreman-Mackey D., Fleming D. P., Lustig-Yaeger J., Deitrick R., 2019, AJ, 157, 64
Maldonado J., et al., 2017, A&A, 598, 27
Mayor M., et al., 2003, The Messenger, 114, 20
Mazeh T., Holczer T., Faigler S., 2016, A&A, 589, 75
Nielsen L. D., et al., 2020, MNRAS, 492, 5399
Otegi J. F., et al., 2021, A&A, 653, 105
Pepe F., et al., 2002, The Messenger, 110, 9
Ricker G. R. et al., 2015, Journal of Astronomical Telescopes, Instruments, and Systems, 1, 014003
Salvatier J., Wieckiâ T. V., Fonnesbeck C., 2016, PyMC3: Python probabilistic programming framework, Astrophysics Source Code Library, ascl:1610.016
Santos N. C., et al., 2002, A&A, 392, 215
Santos N. C., et al., 2013, A&A, 556, 150
Scargle J. D., 1982, ApJ, 263, L835
Schlegel D. J., Finkbeiner D. P., Davis M., 1998, ApJ, 500, L525
Scott N. J., et al., 2021, Frontiers in Astronomy and Space Sciences, 8, 138
Skrutskie M. F., et al., 2006, AJ, 131, 1163
Smith J. C., et al., 2012, PASP, 124, 1000
Sneden C. A., 1973, PhD thesis, THE UNIVERSITY OF TEXAS AT AUSTIN.
Sousa S. G., 2014, in Niemczura E., B. Smalley, W. Pych, eds, Determination of Atmospheric Parameters of B, A, F and G Type Stars. Springer, Cham, p. 297
Sousa S. G., Santos N. C., Israelian G., Mayor M., Monteiro M. J. P. F. G., 2007, A&A, 469, 783
Sousa S. G., et al., 2008, A&A, 487, 373
Sousa S. G., Santos N. C., Adibekyan V., Delgado-Mena E., Israelian G., 2015, A&A, 577, 67
Sousa S. G., et al., 2021, A&A, 656, 53
Stassun K. G., Torres G., 2016, AJ, 152, 180
Stassun K. G., Torres G., 2021, ApJ, 907, L33
Stassun K. G., Collins K. A., Gaudi B. S., 2017, AJ, 153, 136
Stassun K. G., Corsaro E., Pepper J. A., Gaudi B. S., 2018, AJ, 155, 22
Stassun K. G., et al., 2019, AJ, 158, 138
Stumpe M. C., et al., 2012, PASP, 124, 985
Stumpe M. C., Smith J. C., Catanzarite J. H., Van Cleve J. E., Jenkins J. M., Twicken J. D., Girouard F. R., 2014, PASP, 126, 100
Szabó G. M., Kiss L. L., 2011, ApJ, 727, L44
Torres G., Andersen J., Giménez A., 2010a, A&A Rev., 18, 67
Torres G., Andersen J., Giménez A., 2010b, A&A Rev., 18, 67
Twicken J. D., Chandrasekaran H., Jenkins J. M., Gunter J. P., Girouard F., Klaus T. C., 2010, in Software and Cyberinfrastructure for Astronomy. 7740. p. 77401U
Twicken J. D., et al., 2018, PASP, 130, 064502
VanderPlas J. T., 2018, ApJS, 236, 16
Vehtari A., Gelman A., Gabry J., 2017, Statistics and Computing, 27, 1413
Veras D., Mustill A. J., Bonsor A., Wyatt M. C., 2013, MNRAS, 431, 1686
Watanabe S., 2010, Journal of Machine Learning Research, 11, 3571
Weiss L. M., Millholland S. C., Petigura E. A., Adams F. C., Batygin K., Bloch A. M., Mordasini C., 2022, In Protostars and Planets VII, preprint (arXiv:2203.10076)
Wittenmyer R. A., Bergmann C., Horner J., Clark J., Kane S. R., 2019, MNRAS, 484, 4230
Wright E. L., et al., 2010, AJ, 140, 1868
da Silva L., et al., 2006, A&A, 458, 609

APPENDIX A: HARPS SPECTROSCOPY

[1]*Department of Physics, University of Warwick, Coventry CV4 7AL, UK*

Table A1. HARPS spectroscopy.

Time [BJD − 2457000]	RV	σ_{RV}	FWHM [m s^{-1}]	σ_{FWHM}	Contrast	Bis span	S_{MW}	*Ha*
2358.879	54939.1291	1.7636	9116.2436	1.6357	33.8180	28.8576	0.0939	0.1816
2359.889	54942.2963	1.8403	9120.0475	1.6576	33.8104	39.9679	0.0952	0.1776
2360.895	54941.4163	1.9099	9116.7254	2.3186	33.7439	28.4139	0.0929	0.1771
2361.823	54947.1419	1.9352	9119.1708	1.9099	33.7593	39.5333	0.0945	0.1767
2368.779	54936.1522	1.4481	9116.7558	1.7636	33.7817	35.7092	0.0961	0.1808
2368.892	54938.6397	1.4729	9112.4784	1.8159	33.7737	35.3361	0.0976	0.1771
2369.822	54941.4063	1.7946	9118.8143	1.5630	33.7737	31.2242	0.0950	0.1767
2369.901	54943.1930	2.7717	9111.5158	1.5019	33.7755	32.1908	0.0965	0.1773
2370.791	54946.6359	2.1584	9119.6451	1.7115	33.8064	30.9872	0.0948	0.1759
2370.916	54948.0868	1.7343	9112.1726	2.0355	33.8194	38.4706	0.0926	0.1768
2371.810	54947.3120	2.1132	9119.1244	1.5953	33.7795	33.1299	0.0950	0.1812
2371.890	54945.3488	2.4833	9123.6366	1.5901	33.8088	34.4833	0.0929	0.1815
2372.771	54948.3852	2.9147	9118.4646	1.9352	33.8020	40.1501	0.0922	0.1812
2372.896	54946.2718	2.7934	9117.4986	1.6977	33.8151	33.1816	0.0969	0.1818
2376.863	54947.9693	1.5630	9119.9399	1.7149	33.7617	41.4132	0.0975	0.1820
2378.821	54951.3024	2.0355	9107.8579	1.6013	33.7624	37.8135	0.0971	0.1769
2405.829	54938.4662	2.2880	9124.1644	1.8716	33.7738	39.6036	0.0950	0.1820
2409.794	54946.2449	1.8159	9102.3543	2.4664	33.8562	25.0392	0.1001	0.1834
2412.796	54945.5650	1.7984	9126.1584	1.6767	33.7726	28.3786	0.0964	0.1818
2419.683	54954.3765	1.8323	9122.0819	2.1584	33.6817	37.0738	0.0968	0.1827
2419.789	54956.1376	1.6042	9113.9300	1.7343	33.7186	37.8870	0.0959	0.1820
2421.707	54943.2344	1.4407	9126.5836	2.1132	33.7816	34.4838	0.0946	0.1771
2421.806	54947.2486	1.7179	9131.7791	2.4833	33.7808	36.0406	0.0952	0.1770
2422.712	54945.2644	2.5884	9132.1542	2.9147	33.7533	35.6213	0.0899	0.1826
2422.800	54945.6395	1.9274	9134.2216	2.7934	33.7735	43.7364	0.0956	0.1815
2422.935	54942.7393	2.7407	9114.8738	2.5884	33.7706	35.6914	0.0915	0.1817
2423.842	54941.5699	1.5777	9116.5795	1.9274	33.7454	37.4534	0.0947	0.1819
2423.902	54942.5696	2.0993	9133.7634	2.7407	33.7231	33.5343	0.0921	0.1775
2424.785	54948.8373	1.6977	9117.0484	2.0096	33.7747	26.9491	0.0998	0.1783
2425.677	54953.2174	2.0096	9119.6364	2.1990	33.7880	32.6183	0.0971	0.1787
2425.794	54948.1586	2.1990	9109.2590	1.8323	33.7758	35.9231	0.0987	0.1820
2429.803	54944.2671	2.4664	9119.3548	1.6042	33.7349	30.1954	0.0972	0.1804
2443.632	54948.4897	1.5019	9133.8345	2.0077	33.7390	38.6013	0.0981	0.1761
2443.730	54946.2780	1.7115	9120.9396	1.5777	33.7542	28.5068	0.0941	0.1802
2444.647	54947.6991	2.8436	9122.2819	2.0993	33.7997	29.5741	0.0958	0.1811
2444.727	54952.9344	3.0458	9109.2394	1.7946	33.7825	27.8161	0.0935	0.1818
2449.604	54943.1374	2.0077	9104.2840	2.7717	33.7045	36.4253	0.0930	0.1806
2460.746	54941.9471	1.6576	9118.0781	2.2880	33.7604	32.3109	0.0967	0.1798
2461.767	54949.5535	1.7149	9125.4479	3.1523	33.7601	35.3355	0.0987	0.1807
2462.793	54945.9223	1.6357	9124.2665	2.2858	33.7449	27.4409	0.0952	0.1812
2463.802	54948.8167	1.8716	9122.9704	3.3019	33.7807	45.4873	0.0962	0.1752
2464.744	54946.3708	1.6013	9111.8036	2.6251	33.8372	31.8717	0.0916	0.1789
2467.665	54939.5406	2.5859	9114.6408	1.4407	33.7794	33.4307	0.0974	0.1811
2471.654	54941.8031	1.9095	9120.8601	1.7179	33.7775	37.4413	0.0975	0.1815
2473.559	54941.1851	1.5953	9108.0420	1.4481	33.7786	29.5206	0.0994	0.1817
2473.609	54944.5064	1.5901	9122.1321	1.4729	33.7577	28.3784	0.0995	0.1818
2474.613	54944.8060	2.3186	9130.5444	1.7984	33.7461	30.6980	0.0982	0.1825
2475.583	54940.0604	1.8033	9111.5859	1.8403	33.7598	24.7552	0.0992	0.1776
2476.602	54938.6456	2.2858	9128.9792	2.8436	33.5903	39.6079	0.0982	0.1829
2477.579	54935.1412	3.3019	9116.9772	3.0458	33.6390	30.4956	0.0962	0.1800
2477.694	54933.4389	2.6251	9124.6195	1.8033	33.7387	30.3916	0.0986	0.1819
2478.739	54939.0504	3.1523	9112.7792	1.9095	33.7201	40.3934	0.0980	0.1817
2479.654	54941.7172	1.6767	9124.1326	2.5859	33.7251	37.7955	0.1023	0.1830

[2]*Centre for Exoplanets and Habitability, University of Warwick, Gibbet Hill Road, Coventry CV4 7AL, UK*
[3]*Instituto de Astrofísica e Ciências do Espaço, Universidade do Porto, CAUP, Rua das Estrelas, 4150-762 Porto, Portugal*
[4]*Laboratoire d'Astrophysique de Marseille, Pole de l'Etoile Site de Chateau-Gombert, 38 Rue Frederic Joliot-Curie, Marseille 13338, France*
[5]*NASA Ames Research Center, Moffett Field, CA 94035, USA*
[6]*Institute for Computational Science, Center for Theoretical Astrophysics & Cosmology, University of Zurich, Winterthurerstr. 90, 8057 Zurich, Switzerland*
[7]*Department of Physics and Astronomy, Vanderbilt University, Nashville, TN 37235, USA*
[8]*Centre for Space Domain Awareness, University of Warwick, Gibbet Hill Road, Coventry CV4 7AL, UK*
[9]*Department of Astronomy of the University of Geneva, Geneva Observatory, Chemin Pegasi 51, 1290 Versoix, Switzerland*
[10]*Department of Physics and Kavli Institute for Astrophysics and Space Research, Massachusetts Institute of Technology, Cambridge, MA 02139, USA*
[11]*Caltech/IPAC, Mail Code 100-22, 1200 E. California Blvd. Pasadena, CA 91125, USA*
[12]*Center for Astrophysics | Harvard & Smithsonian, 60 Garden Street, Cambridge, MA 02138, USA*
[13]*Centro de Astrobiología (CAB, CSIC-INTA), Depto. de Astrofísica, ESAC campus, 28692, Villanueva de la Cañada (Madrid), Spain*
[14]*European Southern Observatory, Karl-Schwarzschild-Straße 2, 85748 Garching bei München, Germany*
[15]*Physikalisches Institut, University of Bern, Gesellsschaftstrasse 6, 3012 Bern, Switzerland*
[16]*Space Telescope Science Institute, 3700 San Martin Drive, Baltimore, MD 21218, USA*
[17]*Departamento de Física e Astronomia, Faculdade de Ciências, Universidade do Porto, Rua do Campo Alegre, 4169-007 Porto, Portugal*
[18]*Department of Earth, Atmospheric and Planetary Sciences, Massachusetts Institute of Technology, Cambridge, MA 02139, USA*
[19]*Department of Aeronautics and Astronautics, Massachusetts Institute of Technology, 77 Massachusetts Avenue, Cambridge, MA 02139, USA*
[20]*SETI Institute, Mountain View, CA 94043, USA*
[21]*Department of Astrophysical Sciences, Princeton University, Princeton, NJ 08544, USA*

This paper has been typeset from a TEX/LATEX file prepared by the author.